Sensitivity-Tunable Temperature SPR Sensor Based on Side-Opening Grapefruit Fiber With Liquid Mixture

Xianxing Ji, Nannan Luan, Donglian Hou, Wandi Zhang, Xia Jiang, Zhiwei Zhang, Li Song, Yaoyao Qi, and Jianfei Liu

***Abstract*—We demonstrate a sensitivity-tunable temperature SPR sensor based on side-opening grapefruit fiber. The opening sections of the fiber are coated with gold layer and then filled with a liquid mixture of ethanol and chloroform as the sensing medium. The variation of the temperature will lead to different coupling efficiencies between the core-guided mode and the plasmonic mode, and then resulting in the change of loss spectra of the fiber that will be detected. Simulation results indicate that the temperature sensitivity of the sensor is 19.9 nm/°C at 10°C when the volume fraction of ethanol in the mixture is 0.1. Moreover, by adjusting the volume fraction, the sensitivity of proposed sensor can achieve the upper limit for a certain temperature range without the excitation of higher order plasmonic modes.**

***Index Terms*—Microstructured optical fiber, optical fiber sensor, surface plasmon resonance, temperature sensor.**

I. Introduction

SURFACE plasmon resonance (SPR) is the phenomenon that electromagnetic waves resonance with surface plasmon polaritons (SPP) under the specific conditions in optical frequencies, which is sensitive to the change in the refractive index (RI) of the dielectric at the metal/dielectric interface, and therefore being applied in many optical sensors [1]. The optical fiber sensors based on SPR have been proven to successfully used in various sensing applications such as traditional immunoassays (ELISA, DNA detection, etc.), clinical diagnosis, drug discovery, environmental monitoring and so on [1]–[5]. However, those conventional optical fiber-based SPR sensors generally exist phase matching problem, which is the major cause of low sensitivity of those sensors [6]–[12]. This problem can be alleviated by using microstructured optical fibers (MOFs) that could tune the effective RI of the core-guided modes reach to the anticipated values [6]–[12]. In addition, the used MOFs with their flexible design structures can also supply the desired advantages such as stable, optimized optical field distribution and controllable dispersion characteristics [6]–[12]. Those MOF-based SPR sensor designs can detect not only the RI changes of the analyte, but also the temperature changes by replacing the analytes with the sensing medium possess large thermos-optic coefficient [13]–[16]. Compared with other optical fiber temperature sensors, such as FMF-SCF (few mode fiber- seven core fiber) structure (91.8 pm /°C) [17], fiber Bragg grating (FBG) structure (139 pm/°C) [18] and hybrid mechanism structure (42.18pm/°C and 2.057 nm/°C) [19], the advantages of MOF-SPR temperature sensors are higher sensitivity and tunable sensitivity range by choosing the sensing medium [13]–[16]. However, to realize SPR for temperature sensing, the micron-sized air holes of those MOF need to be coated with metal films or filled with metal nanowires by numerous complex and precise processes [13]–[16]. In addition, the sensing medium also needs to be filled into the fiber holes. In general, these processing procedures are very hard to be controlled and make it difficult to change the sensing medium, which can be used to effectively tune the sensitivity and sensing range [13], [15].

Recently, the opening MOFs, including exposed-core MOFs, side-opening MOFs and side-polishing MOFs, are employed to develop SPR sensors to solve the fabrication problems above [20]–[38]. The opening portion of those MOFs acting as the sensing channel not only can be easy to be coated with metal film but also provide convenience for analyte changing. Taking advantages of the opening MOFs, in this work, we design a sensitivity-tunable SPR temperature sensor based on side-opening grapefruit fiber. A liquid mixture of ethanol and chloroform is used as the sensing medium. Changing the volume fraction of the component in the mixture can flexibly alter its actual thermo-optic coefficient and the RI, and thus tuning the temperature sensitivity and sensing range of the proposed sensor.

II. Structure and Theory

Grapefruit fibers [13], as shown in Fig. 1(a), have six large air-holes in its cladding. In our sensor design, the part of the cladding outside the air-hole should be cut a slot to expose the hole to the external environment, and thus can be easily coated with the gold layer and then immersed in the liquid mixture (sensing medium). The 3D and 2D views of the resulting structure are shown in Fig. 1(b) and (c), respectively. Cutting

Manuscript received March 24, 2022; accepted April 2, 2022. Date of publication April 5, 2022; date of current version April 27, 2022. This work was supported by the Natural Science Foundation of Hebei Province under Grants F2019202294, F2019202252, and F2019202467. (*Corresponding author: Nannan Luan.*)

The authors are with the Tianjin Key Laboratory of Electronic Materials and Devices, School of Electronics and Information Engineering, Hebei University of Technology, Tianjin 300401, China (e-mail: 202021902017@stu.hebut.edu.cn; nannanluan@gmail.com; 201921902013@stu.hebut.edu.cn; 202131903016@stu.hebut.edu.cn; xunjiang@hebut.edu.cn; zhangzhiwei@hebut.edu.cn; songli@hebut.edu.cn; qiyao@hebut.edu.cn; jfliu@hebut.edu.cn).

Digital Object Identifier 10.1109/JPHOT.2022.3165039

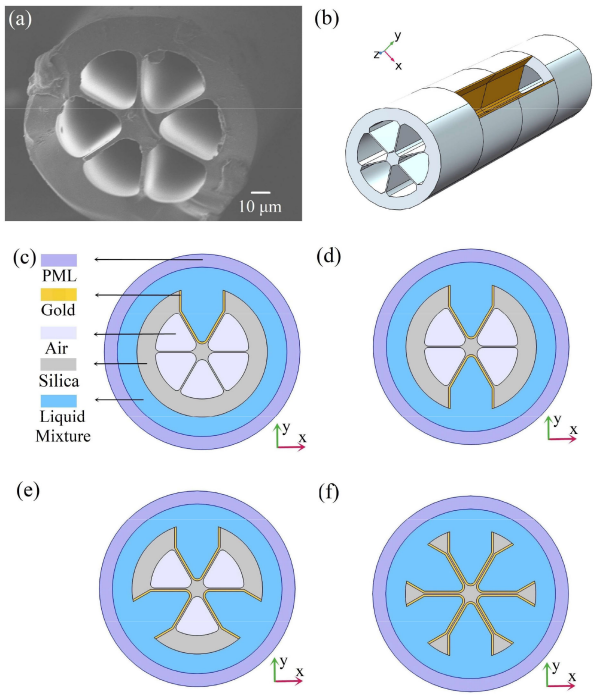

Fig. 1. (a) Scanning electron image (SEM) [39] of the grapefruit fiber, (b) 3-D view of the SPR temperature sensor based on the grapefruit fiber with one opening hole, (c)-(f) Cross-section view of the SPR temperature sensor based on the grapefruit fiber with one, two, three and six opening holes.

open the air-holes of the fiber can be manufactured by some mature methods, such as mechanically polishing, chemically etching, focused ion beam [40], femtosecond laser micromachining [41], [42] and so on [43], [44]. And coating with the gold film can be realized by using the technologies of electroless plating and high-pressure chemical vapor deposition [45]–[47]. A liquid mixture that comprised of ethanol and chloroform is employed as the sensing medium to tune the thermo-optic coefficient and the RI in temperature sensing. We investigate the sensing performances of four feasible structures, as shown in Fig. 1(c)–(f), which with the number of the opening holes (N) is 1, 2, 3 and 6, respectively.

Here we use COMSOL Multiphysics software with finite element method (FEM) to find complex propagation constants of the guided modes, and employ the perfect matched layer (PML) boundaries to match the outmost layer. In the FEM modeling, the diameters of the cladding, air-holes and core area are 125μm, 34.6μm and 12μm, respectively. The distance between the centers of the neighbor air-hole is 35.3μm, and the thickness of the gold layer (m) is 40 nm. All the computation areas are discretized by the triangular normal mesh.

For the material parameters, the default value of air RI is 1. In the case of the MOF, we consider the fused silica as the background material. And its RI (n) is calculated by the dispersion equation [48]:

$$\begin{aligned} n^2(\lambda,T) &= (1.31552 + 0.690754 \times 10^{-5}T) \\ &+ \frac{(0.788404 + 0.235835 \times 10^{-4}T)\lambda^2}{\lambda^2 - (0.0110199 + 0.584758 \times 10^{-6}T)} \\ &+ \frac{(0.91316 + 0.548368 \times 10^{-6}T)\lambda^2}{\lambda^2 - 100} \end{aligned} \tag{1}$$

where the unit of wavelength λ and temperature T are microns and degrees Celsius, respectively. The dielectric function of the gold $\varepsilon(\omega)$ can be calculated by the Drude-Lorentz model [10]:

$$\varepsilon(\omega) = \varepsilon_1 + i\varepsilon_2 = \varepsilon_\infty - \frac{\omega_p^2}{\omega(\omega + i\omega_c)} \tag{2}$$

where the $\omega_{\rm p}$ is the plasma frequency and its value is 1.3659×10^{16}, the $\omega_{\rm c}$ is the collision frequency and its value is 1.45×10^{14}, and the ω_∞ is related to absorption peaks in high-frequency section and its value is 9.75 [49].

In addition, the $\omega_{\rm p}$ influenced by the temperature changing can be calculated by [50]:

$$\omega_{\rm p} = \omega_{p0} \times \exp\left(-\frac{T - T_0}{2} \times \alpha_V(T_0)\right) \tag{3}$$

where the $\omega_{\rm p0}$ is the plasma frequency at T_0 that is the room temperature (298.15K), and the $\alpha_V(T_0)$ is the coefficient of thermal expansion for metal.

The collision frequency $\omega_{\rm c}$ is related to phonon-electron scattering frequency ($\omega_{\rm cp}$) and electron-electron scattering frequency ($\omega_{\rm ce}$), and their relationship can be shown as [51], [52]:

$$\omega_{\rm c} = \omega_{\rm cp} + \omega_{\rm ce} \tag{4}$$

The $\omega_{\rm ce}$ changed by the temperature can be represented by the Lawrence model [53]:

$$\omega_{\rm ce}(T) = \frac{1}{6}\pi^4 \frac{\Gamma\Delta}{hE_F}\left[(k_B T)^2 + \left(\frac{h\omega}{4\pi^2}\right)^2\right] \tag{5}$$

where Γ is the dimensionless number [53], Δ is fractional umklapp scattering and h, E_F, k_B are Planck constant, Boltzmann constant, metal electrons Fermi energy, respectively. For gold, we take $\Gamma = 0.55$, $\Delta = 0.77$, $h = 6.626\times10^{-34}$Js, $E_F = 5.51$eV, $k_B = 1.38\times10^{-23}$J/K [53].

The $\omega_{\rm cp}$ is also affected by the temperature, and can be described by the Holstein model [54]:

$$\omega_{cp}(T) = \omega_0\left[\frac{2}{5} + 4\left(\frac{T}{T_D}\right)^5 \int_0^{T_D/T} \frac{z^4 dz}{{\rm e}^z - 1}\right] \tag{6}$$

where T_D is Debye temperature, and the units of T and T_D are both degree Kelvins. The ω_0 is a constant include the ion density, ion mass, isolated atom's total scattering cross section, and other common constants [54]. For ω_0, we use the method summarized in [14] to calculate it indirectly.

Therefore, the Eqs 2–6 could be used to derive the dielectric function of the gold depending on the frequency and the temperature. It is important to note that using the method of linear formula for bulk metal is not applicable here to calculate the thermal expansion of the metal film. Because for the metal film, it may only expand along the normal direction. Therefore, the corresponding thermal expansion coefficient (α'_L) is employed to obtain the correct thickness of the expanded film and it can be written as [55]:

$$\alpha'_L = \alpha_L \frac{1+\mu}{1-\mu} \tag{7}$$

where α_L is the linear thermal expansion coefficient and $\alpha_L = \alpha_V/3$, μ is the Poisson number of the metal. The values of α_V and μ are 4.26×10^{-5} and 0.44, respectively [14].

TABLE I
FITTING PARAMETERS OF CAUCHY FORMULA FOR ETHANOL AND CHLOROFORM AT 20°C [49]

	Ethanol	Chloroform
C_0	1.83347±0.00199	2.05159±0.00100
$C_1(\mu m^2)$	0.00648±0.00138	0.01005±0.00069
$C_2(\mu m^4)$	0.00031±0.00025	0.00059±0.00013
$C_3(\mu m^{-2})$	−0.00352±0.00071	−0.00052±0.00035

To enhance the sensitivity of the sensor for the temperature sensing, the ethanol and chloroform are chosen and mixed as the sensing medium in this design. The introduction of ethanol is aiming to lower the RI of the sensing medium, since chloroform has the characteristics of large RI that can excite higher order plasmonic modes which may introduce noises in SPR spectra [11], [13]–[15].

For the liquid mixture composed of the two substances, its RI can be represented by the Eq. (8) of the mixture rule in [56]:

$$\frac{n_{\text{mix}}^2-1}{n_{\text{mix}}^2+2}=\varphi_1\frac{n_1^2-1}{n_1^2+2}+\varphi_2\frac{n_2^2-1}{n_2^2+2} \tag{8}$$

where n_{mix} is the RI of liquid mixture, n_1 and n_2 are the RI of ethanol and chloroform. The volume fraction of the two compositions in the liquid mixture are φ_1 and φ_2, respectively. Therefore, φ_1 can be replaced by 1-φ_2.

The individual RI of ethanol and chloroform, at the temperature of $T_C = 20$°C, can be computed by using the Cauchy formula [57]:

$$n_0^2(\lambda) = C_0 + \frac{C_1}{\lambda^2} + \frac{C_2}{\lambda^4} + C_3\lambda^2 \tag{9}$$

where C_0, C_1, C_2, and C_3 are fitting parameters of Cauchy formula. It has been proved that the 4 terms of Cauchy formula have a better fitting result than the two items used in the Sellmeier formula [57]. The fitting parameters of alcohol and chloroform are shown in the Table I [57].

At other temperatures, the individual RI of the liquid has an approximate linear relationship with the temperature behavior, which can be evaluated by [58]:

$$n_T = n_0 + (dn/dT)(T - T_C) \tag{10}$$

where n_0 is the RI given by Cauchy formula, T is the temperature in degrees Celsius. The thermo-optical coefficients *dn/dT* amount to -3.940 $\times 10^{-4}$/°C for ethanol and -6.328$\times 10^{-4}$/°C for chloroform [59], [60].

III. RESULTS

Fig. 2 shows loss spectra of the *x*- and *y*-polarized core-guided modes of the structure with $N = 1$ at 0°C and 10°C when m is 40 nm and volume fraction of the ethanol (φ_1) is 0.3. For this structure in FEM modeling, the complete mesh consists of 45042 domain elements and 3542 boundary elements. As shown in Fig. 2(b), for example, the resonance peak (λ_{peak}) of the *y*-polarized core-guided mode is observed at 939 nm (dot B) for 10°C. This is on account of the energy transfer from the

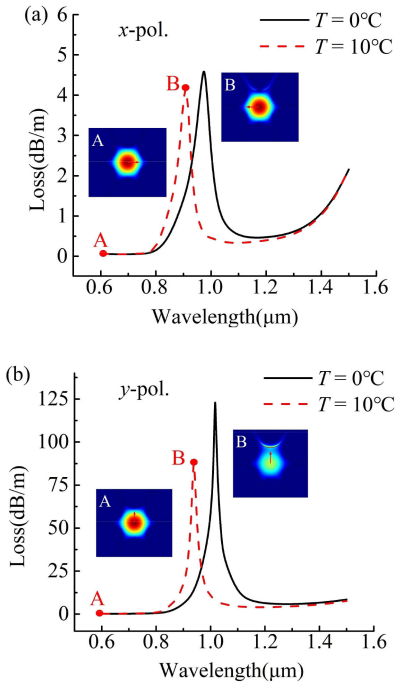

Fig. 2. Loss spectra of the (a) *x*-polarized and (b) *y*-polarized core-guided modes of the structure with $N = 1$ and $m = 40$ nm. Insets show the E field distributions of the corresponding core-guided modes.

y-polarized core-guided mode into the lossy plasmonic mode [20]. The electric field (E field) distributions of the *y*-polarized core-guided modes [insets A and B] in Fig. 2(b) obvious display the processes of energy transfer between the two modes. The energy is mainly confined in the core area at nonresonance wavelength as the inset A shown in Fig. 2(b). While part of that transfer into the plasmonic mode at the resonance wavelength, as seen from the inset B in Fig. 2(b) where the bright portion near the top of the core area is the energy of the plasmonic mode. From Fig. 2, it is worthy to note that the losses at the *y*-polarized resonance peak is many times higher than that at *x*-polarized resonance peak because the *y*-polarized core-guided modes with the electric field orthogonal to the gold surface can couple better with the plasmonic modes [20], [61]. This feature indicates that monitoring the *y*-polarized core-guided modes can obtain narrower resonance spectral and better signal to noise ratio in the wavelength interrogation.

Figs. 3– 5 present loss spectra of the *x*- and *y*-polarized core-guided modes of the structure with $N = 2$, 3 and 6 when other conditions remain consistent with the above structure mentioned in Fig. 2. From the data in Fig. 3–5, it can be seen that the processes of energy transfer for structure with multi opening holes are similar to that of structure with one opening hole. However, there was a significant difference among the four structures that the more opening holes they have, the narrower resonance spectral will be found. This is owing to the metal layer coated on several opening hole areas could allow more plasmonic modes to be excited and thus more energy transfer between the core-guided modes and plasmonic modes as the insets B shown in Fig. 2 and insets A shown in Figs. 3–5.

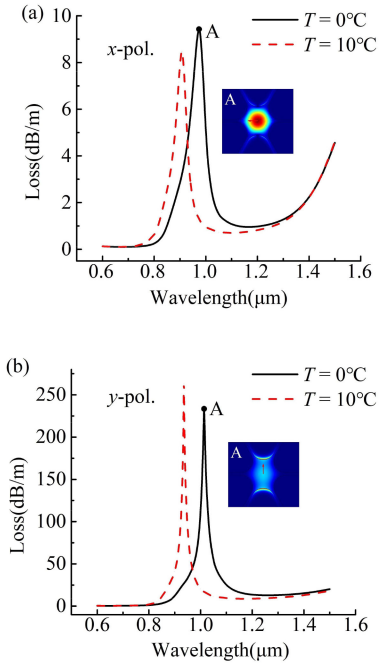

Fig. 3. Loss spectra of the (a) *x*-polarized and (b) *y*-polarized core-guided modes of the structure with $N = 2$ and $m = 40$ nm. Insets show the E field distributions of the core-guided modes at resonance wavelength for $T = 0$°C.

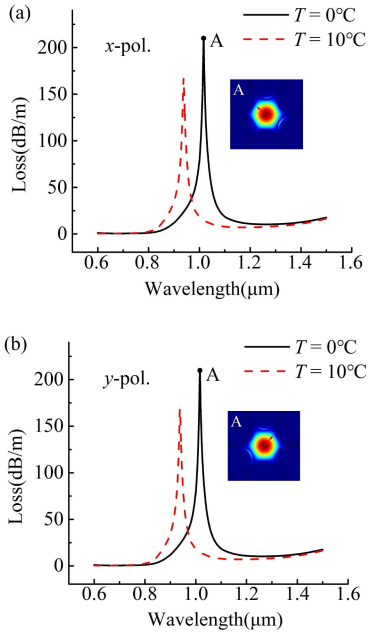

Fig. 4. Loss spectra of the (a) *x*-polarized and (b) *y*-polarized core-guided modes of the structure with $N = 3$ and $m = 40$ nm. Insets show the E field distributions of the core-guided modes at resonance wavelength for $T = 0$°C.

Besides, it is important to note that a small peak located at 904 nm (dot B) could be observed in Fig. 5(b). One reason for this phenomenon is that there exists the interference between the neighboring hole of the structure. The other is due to the fact that higher order plasmonic modes are excited and, in consequence, coupled with core modes, which could be observed from insets B in Fig. 5(b).

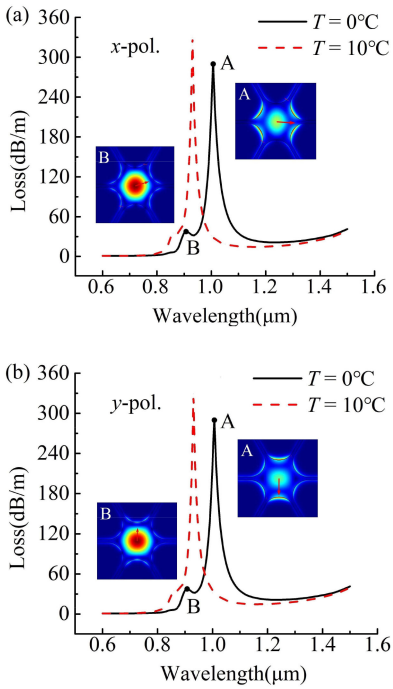

Fig. 5. Loss spectra of the (a) x-polarized and (b) y-polarized core-guided modes of the structure with $N = 6$ and $m = 40$ nm. Insets show the E field distributions of the corresponding core-guided modes.

To calculate the temperature sensitivity of the proposed sensors, we employ a spectrum-based detection method. And the sensitivity (S_λ) could be written as [6], [14]:

$$S_\lambda[\mathrm{nm}/^\circ C] = \frac{d\lambda_{\mathrm{peak}}(T)}{dT} \tag{11}$$

where dT is the temperature variation and $d\lambda_{\mathrm{peak}}$ is moving distance of resonance wavelength correspond to dT. By using the data of Fig. 3, we can calculate that the spectral sensitivity of the *x*- and *y*-polarized is 6.7 nm/°C and 7.9 nm/°C in the detection range of 0°C to 10°C for the structure with $N = 2$ when φ_1 is 0.3. In addition, the temperature sensitivity of *x*- and *y*-polarized core guided modes for the four structures at different temperatures are shown in Table II under the condition of $\varphi_1 = 0.3$. The N denotes the number of the opening holes of the sensor structures in this table.

From Table II, it can be seen that, for the structure with $N = 1$ or 2, the temperature sensitivities of *y*-polarized resonance peaks are higher than that of *x*-polarized resonance peaks at the same temperature range, because resonance effects of *y*-polarized resonance peaks are better than that of *x*-polarized resonance peaks as shown in Figs. 2 and 3. While, for the structure with $N = 3$ or 6, the sensitivities of *x*- and *y*-polarized peaks are very close due to the resonance effects of the two polarized peaks are quite similar, which could be observed in Figs. 4 and 5.

IV. Discussion

The temperature sensors we proposed here possess the following two advantages. One is that it could provide convenience to the fabrication processes for metal coating and sensing media

TABLE II
TEMPERATURE SENSITIVITY OF THE *X*-POLARIZED AND *Y*-POLARIZED CORE GUIDED MODES OF THE FOUR STRUCTURES AT DIFFERENT TEMPERATURES WHEN φ_1 IS 0.3

Temperature (°C)	Sensitivity(nm/°C)							
	$N=1$		$N=2$		$N=3$		$N=6$	
	x-pol.	*y*-pol.	*x*-pol.	*y*-pol.	*x*-pol.	*y*-pol.	*x*-pol.	*y*-pol.
0	6.6	7.8	6.7	7.9	7.9	7.9	7.6	7.5
10	5.2	5.9	5.1	5.8	5.9	5.9	5.8	5.8
20	4.1	4.6	4.1	4.6	4.6	4.6	4.4	4.4
30	3.4	3.8	3.4	3.7	3.8	3.8	3.7	3.7
40	2.9	3.1	3.1	3.1	3	3	3.1	3.1

TABLE III
SENSITIVITY COMPARISON OF VARIOUS FIBER OPTIC TEMPERATURE SENSORS

Fiber Structure	Temperature range (°C)	Wavelength range (nm)	Maximum sensitivity (nm/°C)	Sensitivity tunable	Metallization of fiber holes	Filling into fiber holes with liquid	Ref.
Selectively coated PCF	0–100	500–1000	0.72	No	Yes	Yes	[14]
Grapefruit fiber with nanowires	-4–53	700–1100	4	Yes	No	Yes	[15]
PCF with a liquid core	35–45	1500–2500	9.89	No	Yes	Yes	[16]
Side opening hollow fiber	14.55–51.19	600–1800	4.98	Yes	Yes	Yes	[27]
D-shaped hole fiber	20–50	800–1150	3.635	No	Yes	Yes	[62]
PCF with dual-core	10–70	1400–1800	6.32	No	Yes	Yes	[63]
Square array PCF	0–60	850–1000	10.4	No	Yes	Yes	[64]
Side opening grapefruit fiber	0–50	400–1600	19.9	Yes	No	No	This work

filling due to the employment of the side-opening fiber. The other is that it is able to alter the sensitivity and the detecting range of temperature by tuning the proportion of the component in the liquid mixture. According to the results above, the sensor structure with $N = 2$ at *y*-polarized spectrum-based detection method is the better option to balance the sensing performance and manufacturing difficulty. Therefore, we take *y*-polarized resonance peak in the structure with $N = 2$ as an example to discuss the influences of the volume fraction of liquid mixture and the thickness of gold layer on the sensing performance.

A. Influence of Volume Fraction of Component in the Liquid Mixture on Sensing Performance

According to Eq. 8, when the volume fraction of the ethanol and chloroform are changed, the RI and thermo-optical coefficient (*dn/dT*) of the liquid mixture varies accordingly, thus resulting in different resonance peaks and the sensitivities at the same temperature. Fig. 6(a) exemplarily shows the loss spectra of the *y*-polarized core-guided modes for the structure with $N = 2$ at 40°C when *m* is 40 nm and the volume fraction of the ethanol (φ_1) in the liquid mixture is 0, 0.1, 0.2 and 0.3, respectively. As shown in Fig. 6(a), the resonance peak shows higher value of loss spectra for low φ_1 than that for high φ_1 and its wavelength shifts from 794 nm for $\varphi_1 = 0.4$ to 996 nm for $\varphi_1 = 0$. According to Eq. 8, we could find that this is owing to the reduction of φ_1 increases the RI of the liquid mixture, therefore the contrast of RI for the fiber core and the liquid mixture at the cladding is reduced, and resulting in more energy transferred from core-guided modes into lossy plasmonic modes. In addition, the growth of RI could cause an increase of effective refractive index (n_{eff}) of plasmonic mode, hence the wavelength corresponding to the intersection (phase-matching point) of the n_{eff} curves of plasmonic mode and core mode shifts towards the long wavelength [8]–[11], [13], [14], [29], [37]. This peak behavior at 40°C is similar to that at the other temperatures, and thus leading to different sensitivities for the different φ_1 as shown in Fig. 6(b) that presents the sensitivity curves of the *y*-polarized core-guided modes of the structure with $N = 2$ at the 0–50°C detection range when the m is 40 nm and the φ_1 is 0, 0.1, 0.2, and 0.3, respectively. Overall, the sensitivity

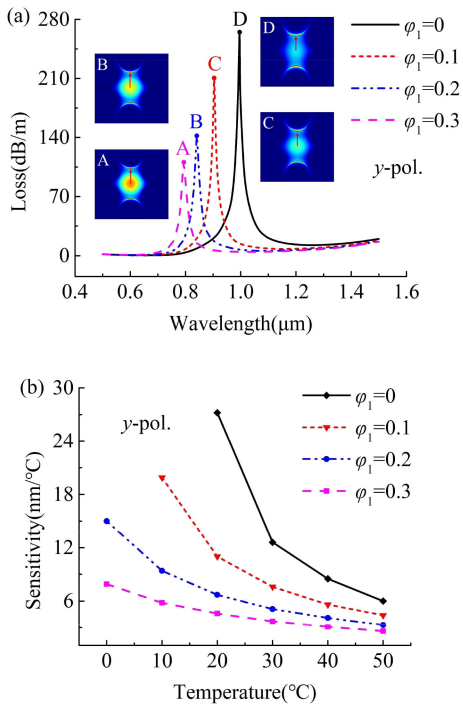

Fig. 6. (a) Loss spectra of the *y*-polarized core-guided modes of the structure with $N = 2$ at 40°C when *m* is 40 nm and φ_1 is 0, 0.1, 0.2 and 0.3, respectively. Insets show the E field distributions of the core-guided modes at resonance wavelength for $\varphi_1 = 0$, 0.1, 0.2 and 0.3. (b) Sensitivity curves of the *y*-polarized core-guided modes of the structure with $N = 2$ when *m* is 40 nm and φ_1 is 0, 0.1, 0.2, and 0.3, respectively.

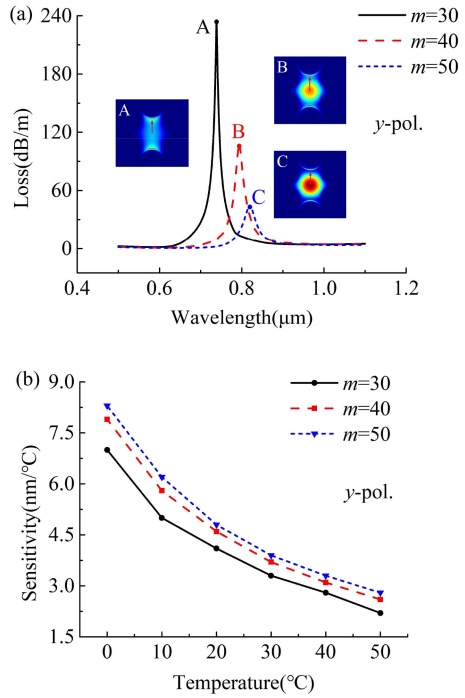

Fig. 7. (a) Loss spectra of the *y*-polarized core-guided modes of the structure with $N = 2$ at 40°C when φ_1 is 0.3 and m is 30 nm, 40 nm and 50 nm, respectively. Insets show the E field distributions of the core-guided modes at resonance wavelength for m = 30 nm, 40 nm and 50 nm. (b) Sensitivity curves of the *y*-polarized core-guided modes of the structure with $N = 2$ when φ_1 is 0.3 and m is 30 nm, 40 nm and 50 nm, respectively.

gradually increases with the decrease of φ_1, especially in low temperature region. Two reasons cause this phenomenon, one reason is that the decrease of φ_1 increases the RI of the liquid mixture at the same temperature and thus the sensitivity, which is consistent with the sensing performance of MOF-SPR sensors for RI and temperature sensing [10], [11], [13], [15], [20], [36]. The other reason is that the reduction of φ_1 also increase dn/dT of liquid mixture and hence leading to a larger RI variation for the same temperature change which could enhance the sensitivity even more. Although reducing φ_1 could increase the sensitivity effectively, when temperature is low and the value of φ_1 is small, the RI of the liquid mixture will reach a higher value and higher order plasmonic modes also could be excited and coupled with the core modes, thus making the detection more difficult [10], [11], [13]–[15], [20]. This is the reason why we can observe in Fig. 6(b) that the lower detection limit of the temperature only reaches to 20°C and 10°C when φ_1 value is 0 and 0.1, respectively. Therefore, for detection of a certain temperature range, the φ_1 should be adjusted to an appropriate value to ensure that the sensor can work effectively, and meanwhile obtain the maximum sensitivity.

B. Influence of Thickness of Gold Layer on Sensing Performance

Surface plasmon waves are very sensitive to the thickness of the metallic layer [8]–[11], [13], [14]. Fig. 7(a) shows the effect of m on loss spectra of *y*-polarized core-guided modes of the structure with $N = 2$ at 40°C when φ_1 is 0.3 and the m is 30 nm, 40 nm and 50 nm, respectively. As the m increases, we can observe that the peak wavelength moves to a longer wavelength, and the full width at half maximum (FWHM) increases which means lower resolution in the spectrum-based detection. This is due to the fact that the growth of m could lead to the increase of n_{eff} of plasmonic mode, and thus the phase-matching point determined by the n_{eff} curves of plasmonic mode and core-guided mode shifts to longer wavelength [29], [37]. In the meantime, the increase of m could weaken the energy transfer from core-guided mode into plasmonic mode, as shown in insets A–C of Fig. 7(a), which causes the declining of peak losses and the increasing of FWHM. The shifts of resonance wavelength at 40°C is similar to that at the other temperatures and moves more distance under lower temperature area for the same m changing. Consequently, it leads to the increase of sensitivity when m increases, and this trend can be illustrated by the data in Fig. 7(b), which shows the sensitivity of the *y*-polarized core-guided modes of the sensor when φ_1 is 0.3 and m is 30 nm, 40 nm and 50 nm, respectively, in the detection range of 0°C to 50°C. This phenomenon is identical with that of the MOF-SPR sensor for the RI and temperature sensing which the increase of metallic layer result in movement of the resonance peak towards long wavelength and increasement of the sensitivity [10]–[11], [13], [15], [37].

In general, the proposed SPR temperature sensor with side-opening structure not only avoid the inside coating and filling of the fiber holes and thus lower difficulty in sensor fabrication, but also give the capacity of flexibly tunable sensitivity primarily through changing the volume fraction of ethanol in the liquid mixture (φ_1). Therefore, it is able to provide higher sensitivity at a desired temperature range, as shown in Table III for example, the sensitivity can reach to 19.9 nm/°C at $m = 40$ nm by changing the φ_1 to be 0.1, which is higher than that of other MOF-based SPR sensors that can not adjust sensitivity easily.

V. Conclusion

We propose a SPR temperature sensor based on side-opening grapefruit fiber that filled with liquid mixture of ethanol and chloroform as the sensing medium, which is able to tune the most sensitive range of the sensor to a desired value and avoid the excitation of higher order plasmonic modes. This design combines the advantages of the side-opening MOFs that facilitate the coating of metallic layer and the altering of sensing medium, and of the liquid mixture that its RI and thermo-optical coefficient can be flexibly adjusted. Thus, it is expected to be more competitive in the field of optical fiber temperature sensors.

References

[1] T. Allsop and R. Neal, "A review: Evolution and diversity of optical fibre plasmonic sensors," *Sensors*, vol. 19, no. 22, Nov. 2019, Art. no. 4874.
[2] M. E. Martínez-Hernández, P. J. Rivero, J. Goicoechea, and F. G.Arregui, "Trends in the implementation of advanced plasmonic materials in optical fiber sensors (2010–2020)," *Chemosensors*, vol. 9, no. 4, Mar. 2021, Art. no. 64.
[3] P. Singh, "SPR biosensors: Historical perspectives and current challenges," *Sens. Actuators B Chem.*, vol. 229, pp. 110–130, Jan. 2016.
[4] B. Park *et al.*, "Surface plasmon excitation in semitransparent inverted polymer photovoltaic devices and their applications as label-free optical sensors," *Light: Sci. Appl.*, vol. 3, no. 12, Sep. 2014, Art. no. e222.

[5] J. Lao *et al.*, "In situ plasmonic optical fiber detection of the state of charge of supercapacitors for renewable energy storage," *Light Sci. Appl.*, vol. 7, no. 1, Jul. 2018, Art. no. 11.

[6] B. Gauvreau, A. Hassani, M. F. Fehri, A. Kabashin, and M. Skorobogatiy, "Photonic bandgap fiber-based surface plasmon resonance sensors," *Opt. Exp.*, vol. 15, no. 18, pp. 11413–11426, Jun. 2007.

[7] Y. Zhao, Z. Deng, and J. Li, "Photonic crystal fiber based surface plasmon resonance chemical sensors," *Sens. Actuators B Chem.*, vol. 202, pp. 557–567, Oct. 2014.

[8] A. Hassani and M. Skorobogatiy, "Design criteria for microstructured-optical-fiber-based surface-plasmon-resonance sensors," *J. Opt. Soc. Am. B*, vol. 24, no. 6, pp. 1423–1429, Jun. 2007.

[9] Y. Zhang *et al.*, "Microstructured fiber based plasmonic index sensor with optimized accuracy and calibration relation in large dynamic range," *J. Opt. Soc. Am. B*, vol. 248, no. 18, pp. 4161–4166, Aug. 2011.

[10] A. Hassani and M. Skorobogatiy, "Design of the microstructured optical fiber-based surface plasmon resonance sensors with enhanced microfluidics," *Opt. Exp.*, vol. 14, no. 24, pp. 11616–11621, Dec. 2006.

[11] X. Yu *et al.*, "A selectively coated photonic crystal fiber based surface plasmon resonance sensor," *J. Opt.*, vol. 12, no. 1, Dec. 2010, Art. no. 015005.

[12] L. Zheng *et al.*, "Surface plasmon resonance sensors based on Ag-metalized nanolayer in microstructured optical fibers," *Opt. Laser Technol.*, vol. 43, no. 5, pp. 960–964, Jul. 2011.

[13] N. Luan, R. Wang, Y. Lu, and J. Yao, "Simulation of surface plasmon resonance temperature sensor based on liquid mixture-filling microstructured optical fiber," *Opt. Eng.*, vol. 53, no. 6, Jun. 2014, Art. no. 067103.

[14] Y. Peng, J. Hou, Z. Huang, and Q. Lu, "Temperature sensor based on surface plasmon resonance within selectively coated photonic crystal fiber," *Appl. Opt.*, vol. 51, no. 26, pp. 6361–6367, Sep. 2012.

[15] N. Luan, R. Wang, Y. Lu, and J. Yao, "Surface plasmon resonance temperature sensor based on photonic crystal fibers randomly filled with silver nanowires," *Sensors*, vol. 14, no. 9, pp. 16035–16045, Sep. 2014.

[16] L. Qiang, S. Li, and X. Gao, "Highly sensitive plasmonics temperature sensor based on photonic crystal fiber with a liquid core," *Opt. Commun.*, vol. 427, no. 15, pp. 622–627, Nov. 2018.

[17] C. Zhang *et al.*, "Miniature optical fiber temperature sensor based on FMF-SCF structure," *Opt. Fiber Technol.*, vol. 427, pp. 217–221, Mar. 2018.

[18] A. Leal-Junior, J. Casas, C. Marques, M. J. Pontes, and A. Frizera, "Application of additive layer manufacturing technique on the development of high sensitive fiber bragg grating temperature sensors," *Sensors*, vol. 18, no. 12, Nov. 2018, Art. no. 4120.

[19] W. Ni *et al.*, "Simultaneous implementation of enhanced resolution and large dynamic range for fiber temperature sensing based on different optical transmission mechanisms," *Opt. Exp.*, vol. 26, no. 14, Jul. 2018, Art. no. 18341.

[20] N. Luan, R. Wang, W. Lv, and J. Yao, "Surface plasmon resonance sensor based on exposed-core microstructured optical fibers," *Electron. Lett.*, vol. 51, no. 9, pp. 714–715, Apr. 2015.

[21] E. Klantsataya, A. François, H. Ebendorff-Heidepriem, P. Hoffmann, and T. M. Monro, "Surface plasmon scattering in exposed core optical fiber for enhanced resolution refractive index sensing," *Sensors*, vol. 15, no. 10, pp. 25090–25102, Sep. 2015.

[22] N. Luan and J. Yao, "Surface plasmon resonance sensor based on exposed-core microstructured optical fiber placed with a silver wire," *IEEE Photon. J.*, vol. 8, no. 1, Feb. 2016, Art. no. 4800508.

[23] Y. Zhao, Q. Wu, and Y. Zhang, "Theoretical analysis of high-sensitive seawater temperature and salinity measurement based on C-type microstructured fiber," *Sens. Actuators B Chem.*, vol. 258, pp. 822–828, Dec. 2017.

[24] N. D. Gómez-Cardona, E. Reyes-Vera, and P. Torres, "Multi-plasmon resonances in microstructured optical fibers: Extending the detection range of SPR sensors and a multi-analyte sensing technique," *IEEE Sens. J.*, vol. 18, no. 18, pp. 7492–7498, Jul. 2018.

[25] N. Luan, C. Ding, and J. Yao, "A refractive index and temperature sensor based on surface plasmon resonance in an exposed-core microstructured optical fiber," *IEEE Photon. J,* vol. 8, no. 2, Apr. 2016, Art. no. 4801608.

[26] N. Luan, H. Han, L. Zhao, J. Liu, and J. Yao, "Opening up dual-core microstructured optical fiber-based plasmonic sensor with1 large detection range and linear sensitivity," *Opt. Mater. Exp.*, vol. 9, no. 2, pp. 819–825, Feb. 2019.

[27] L. Zhao, H. Han, N. Luan, J. Liu, L. Song, and Y. Hu, "A temperature plasmonic sensor based on a side opening hollow fiber filled with high refractive index sensing medium," *Sensors*, vol. 19, no. 17, Aug. 2019, Art. no. 3730.

[28] J. N. Dash and R. Jha, "Highly sensitive d shaped PCF sensor based on SPR for near iR," *Opt. Quant. Electron.*, vol. 48, no. 2, Jan. 2016, Art. no. 137.

[29] J. N. Dash and R. Jha, "On the performance of graphene-based D-shaped photonic crystal fibre biosensor using surface plasmon resonance," *Plasmonics*, vol. 10, no. 5, pp. 1123–1131, Feb. 2015.

[30] N. Luan, R. Wang, W. Lv, and J. Yao, "Surface plasmon resonance sensor based on D-shaped microstructured optical fiber with hollow core," *Opt. Exp.*, vol. 23, no. 7, pp. 8576–8582, Apr. 2015.

[31] N. Luan, L. Zhao, Y. Lian, and S. Lou, "A high refractive index plasmonic sensor based on D-shaped photonic crystal fiber with laterally accessible hollow-core," *IEEE Photon. J.,* vol. 10, no. 5, Oct. 2018, Art. no. 6803707.

[32] L. Zhao, H. Han, Y. Lian, N. Luan, and J. Liu, "Theoretical analysis of all-solid D-type photonic crystal fiber based plasmonic sensor for refractive index and temperature sensing," *Opt. Fiber Technol.*, vol. 50, pp. 165–171, Jul. 2019.

[33] J. Wu, C. Dou, and L. Hu, "The D-shape elliptical stoma photonic crystal fiber based on surface plasmon resonance with both filtering and sensing," *Opt. Quantum Electron.*, vol. 53, no. 10, pp. 1–14, Sep. 2021.

[34] A. A. S. Falah, W. R. Wong, and F. R. M. Adikan, "Single-mode eccentric-core D-shaped photonic crystal fiber surface plasmon resonance sensor," *Opt. Laser Technol.*, vol. 145, Jan. 2022, Art. no. 107474.

[35] H. Han *et al.*, "Surface plasmon resonance sensor based on dual-side polished microstructured optical fiber with dual-core," *Sensors*, vol. 20, no. 14, Jul. 2020, Art. no. 3911.

[36] H. Han *et al.*, "A large detection-range plasmonic sensor based on an H-shaped photonic crystal fiber," *Sensors*, vol. 20, no. 4, Feb. 2020, Art. no. 1009.

[37] D. Hou *et al.*, "Surface plasmon resonance sensor based on double-sided polished microstructured optical fiber with hollow core," *IEEE Photon. J.*, vol. 13, no. 4, Aug. 2021, Art. no. 6800408.

[38] Z. Zhang, T. Shen, H. Wu, Y. Feng, and X. Wang, "Polished photonic crystal fiber refractive index sensor based on surface plasmon resonance," *J. Opt. Soc. Am. B*, vol. 38, no. 12, pp. F61–F68, Dec. 2021.

[39] R. Wang, Y. Wang, Y. Miao, and J. Yao, "Thermo-optic characteristics of micro-structured optical fiber infiltrated with mixture liquids," *J. Opt. Soc. Korea*, vol. 17, Jun. 2013, Art. no. 3.

[40] C. M. B. Cordeiro *et al.*, "Towards practical liquid and gas sensing with photonic crystal fibres: Side access to the fibre microstructure and single-mode liquid-core fibre," *Meas. Sci. Technol.*, vol. 18, no. 10, Sep. 2007, Art. no. 3075.

[41] C. J. Hensley, D. H. Broaddus, C. B. Schaffer, and A. L. Gaeta, "Photonic band-gap fiber gas cell fabricated using femtosecond micromachining," *Opt. Exp.*, vol. 15, no. 11, pp. 6690–6695, Jun. 2007.

[42] A. V. Brakel, C. Grivas, M. N. Petrovich, and D. J. Richardson, "Micro-channels machined in microstructured optical fibers by femtosecond laser," *Opt. Exp.*, vol. 15, no. 14, pp. 8731–8736, Aug. 2007.

[43] C. M. B. Cordeiro, E. M. D. Santos, C. H. B. Cruz, C. J. S. D. Matos, and D. S. Ferreiia, "Lateral access to the holes of photonic crystal fibers - selective filling and sensing applications," *Opt. Exp.*, vol. 14, no. 18, pp. 8403–8412, Oct. 2006.

[44] F. M. Cox, R. Lwin, M. C. J. Large, and C. M. B. Cordeiro, "Opening up optical fibres," *Opt. Exp.*, vol. 15, no. 19, pp. 11843–11848, Oct. 2007.

[45] J. A. Harrington, "A review of IR transmitting, hollow waveguides. fiber and integrated optics," *Fiber Integr. Opt.*, vol. 19, no. 3, pp. 211–227, Aug. 2000.

[46] N. Takeyasu, T. Tanaka, and S. Kawata, "Metal deposition deep into microstructure by electroless plating," *Jpn. J. Appl. Phys.*, vol. 44, no. 35, Aug. 2005, Art. no. L1134.

[47] P. J. A. Sazio *et al.*, "Microstructured optical fibers as high-pressure microfluidic reactors," *Science*, vol. 311, no. 5767, pp. 1583–1586, Mar. 2006.

[48] G. Ghosh, M. Endo, and T. Iwasaki, "Temperature-dependent sellmeier coefficients and chromatic dispersions for some optical fiber glasses," *J. Lightw. Technol.*, vol. 12, no. 8, pp. 1338–1342, Aug. 1994.

[49] P. B. Johnson and R. W. Christy, "Optical constants of the noble metals," *Phys. Rev. B*, vol. 6, no. 12, pp. 4370–4379, Dec. 1972.

[50] K. Lin, Y. Lu, Z. Luo, R. Zeng, P. Wang, and H. Ming, "Numerical and experimental investigation of temperature effects on the surface plasmon resonance sensor," *Chin. Opt.*, vol. 7, no. 5, pp. 428–413, May 2009.

[51] R. T. Beach and R. W. Christy, "Electron-electron scattering in the intraband optical conductivity of cu, ag, and au," *Phys. Rev. B*, vol. 16, no. 12, pp. 5277–5284, Dec. 1977.

[52] A. K. Sharma and B. D. Gupta, "Theoretical model of a fiber optic remote sensor based on surface plasmon resonance for temperature detection," *Opt. Fiber Technol.*, vol. 12, no. 1, pp. 87–100, Aug. 2005.
[53] W. E. Lawrence, "Electron-electron scattering in the low-temperature resistivity of the noble metals," *Phys. Rev. B*, vol. 13, no. 1, pp. 5316–5319, Jun. 1976.
[54] T. Holstein, "Optical and infrared volume absorptivity of metals," *Phys. Rev.*, vol. 96, no. 2, pp. 535–536, Oct. 1954.
[55] S. Herminghaus and P. Leiderer, "Surface plasmon enhanced transient thermoreflectance," *Appl. Phys. A*, vol. 51, no. 4, pp. 350–353, Oct. 1990.
[56] W. Heller, "Remarks on refractive index mixture rules," *J. Phys. Chem.*, vol. 69, no. 4, pp. 1123–1129, Apr. 1965.
[57] S. Kedenburg, M. Vieweg, T. Gissibl, and H. Giessen, "Linear refractive index and absorption measurements of nonlinear optical liquids in the visible and near-infrared spectral region," *Opt. Mater. Exp.*, vol. 2, no. 11, pp. 1588–1611, Nov. 2012.
[58] R. Wang *et al.*, "A reflective photonic crystal fiber temperature sensor probe based on infiltration with liquid mixtures," *Sensors*, vol. 13, no. 6, pp. 7916–7925, Jun. 2013.
[59] Y. Yu, X. Li, X. Hong, Y. Deng, and W. Tong, "Some features of the photonic crystal fiber temperature sensor with liquid ethanol filling," *Opt. Exp.*, vol. 18, no. 15, pp. 15383–15388, Jul. 2010.
[60] A. Samoc, "Dispersion of refractive properties of solvents: Chloroform, toluene, benzene, and carbon disulfide in ultraviolet, visible, and near-infrared," *J. Appl. Phys.*, vol. 94, no. 9, pp. 6167–6174, Dec. 2003.
[61] X. Zhang, R. Wang, F. M. Cox, B. T. Kuhlmey, and M. C. J. Large, "Selective coating of holes in microstructured optical fiber and its application to in-fiber absorptive polarizers," *Opt. Exp.*, vol. 15, no. 24, pp. 16270–16278, Nov. 2007.
[62] S. Weng, L. Pei, J. Wang, T. Jing, and L. Jing, "High sensitivity D-shaped hole fiber temperature sensor based on surface plasmon resonance with liquid filling," *Photon. Res.*, vol. 5, no. 2, pp. 103–107, Feb. 2017.
[63] C. Mei, Y. Wu, S. Qiu, J. Yuan, X. Zhou, and K. Long, "Design of dual-core photonic crystal fiber for temperature sensor based on surface plasmon resonance effect," *Opt. Commun.*, vol. 508, Apr. 2022, Art. no. 127838.
[64] Y. Fu, M. Liu, P. Shum, and Y. Qin, "PCF based surface plasmon resonance temperature sensor with ultrahigh sensitivity," *Optik*, vol. 250, Nov. 2021, Art. no. 168345.